Geophysical Journal International

Geophys. J. Int. (2011) **186,** 1404–1414 doi: 10.1111/j.1365-246X.2011.05122.x

Detection of high-frequency tensile vibrations of a fault during shear rupturing: observations from the 2008 West Bohemia swarm

Václav Vavryčuk

Institute of Geophysics, Academy of Sciences, Boční II/1401, 141 00 *Praha* 4, *Czech Republic. E-mail: vv@ig.cas.cz*

Accepted 2011 June 23. Received 2011 June 17; in original form 2011 January 5

SUMMARY

The analysis of 12 earthquakes of magnitudes between 1.7 and 3.7 that occurred in 2008 in West Bohemia, Czech Republic reveals that shear rupturing along a fault is accompanied by weak tensile vibrations of the fault. The vibrations are of a narrow frequency band with frequencies distinctly higher than those of shear rupturing. The tensile vibrations decay slowly in time and often resemble resonant waves. They complicate the radiated *P* waveforms and the *P*-wave radiation pattern. The tensile vibrations can be observed in waveforms in directions near the nodal lines where the dominance of shear-faulting radiation is lost. The tensile vibrations are probably generated by opening of the fault during shear rupturing or by creating a wing tensile crack at the tip of the fault when shear fracturing stops.

Key words: Earthquake dynamics; Earthquake source observations; Body waves; Dynamics and mechanics of faulting.

1 INTRODUCTION

High-frequency complex waveforms radiated by an earthquake source are usually attributed to complex slip and rupture histories caused by heterogeneities on a fault or by complex fault geometry (Aki 1984; Kikuchi & Kanamori 1984; Lay & Wallace 1995). The fault heterogeneities or irregularities cause abrupt changes of shear rupture velocity resulting in radiation of high-frequency waves (Spudich & Frazer 1984; Madariaga *et al*. 2006). The frequency of waves is further affected by the directivity of the earthquake source, manifested by a varying width of the source-time function in dependence on the angle between the directions of radiation and rupture propagation. These effects are mostly observed for large earthquakes (Cohee & Beroza 1994; Wald 1996; Zeng & Chen 2001; Lay *et al*. 2005; Konca *et al*. 2010), but some studies using dense local seismic networks reveal similar behaviour of waves also in moderate or small earthquakes (Mori 1996; Boatwright 2007; Frez *et al.* 2010; Seekins & Boatwright 2010).

Another effect which might contribute to the complexity of the source process and of the radiated waves is the time-dependent deviation of slip from the fault caused by the presence of tensile motions during rupturing. This type of faulting is commonly overlooked even though the occurrence of earthquakes combining shear and tensile motions has been reported (Ross *et al*. 1996; Vavryčuk 2002; Foulger *et al*. 2004). They are detected by non-double–couple (non-DC) components in full moment tensors (Frohlich 1994; Julian *et al*. 1997, 1998; Miller *et al*. 1998) and mostly associated with the presence of high-fluid pressure in the source region. So far, the source models incorporating tensile motions are very simple. They either study the source process in the low-frequency limit or assume a common shear-tensile source-time function (Dufumier & Rivera 1997; Vavryčuk 2001).

The aim of this paper is to study tensile motions during earthquake rupturing in 12 earthquakes with magnitudes of 1.6 to 3.7 that occurred in West Bohemia, Czech Republic, in 2008 (Fischer *et al*. 2010). It is shown that tensile motions are present during rupturing having different frequency and duration than shear motions and that they significantly affect the radiated waves.

2 THE 2008 WEST BOHEMIA EARTHQUAKE SWARM

The West Bohemia/Vogtland region, the border area between the Czech Republic and Germany, is the most seismically active region in the Bohemian Massif (Babuška *et al.* 2007). Active tectonics is manifested by numerous mineral springs, emanations of CO_2, presence of Tertiary or Quaternary volcanism, and by persistent seismic activity with frequent occurrence of earthquake swarms. The most prominent earthquake swarms occurred recently in 1985/86 (Vavryčuk 1993), in 1997 (Vavryčuk 2002) and in 2000 (Fischer 2003; Fischer & Horálek 2003). Their duration was between 2 weeks to 2 months and the activity was focused typically at depths ranging from 7 to 12 km. The strongest instrumentally recorded earthquake was the *M* 4.6 earthquake on 1985 December 21. The last extensive earthquake swarm occurred in October 2008 (Fischer *et al*. 2010).

The 2008 earthquake swarm lasted for 4 weeks and involved about 25.000 microearthquakes with magnitude higher than −0.5. Nine earthquakes reached magnitude higher than 3.0. The largest earthquake had a magnitude of 3.7. The epicentres formed a

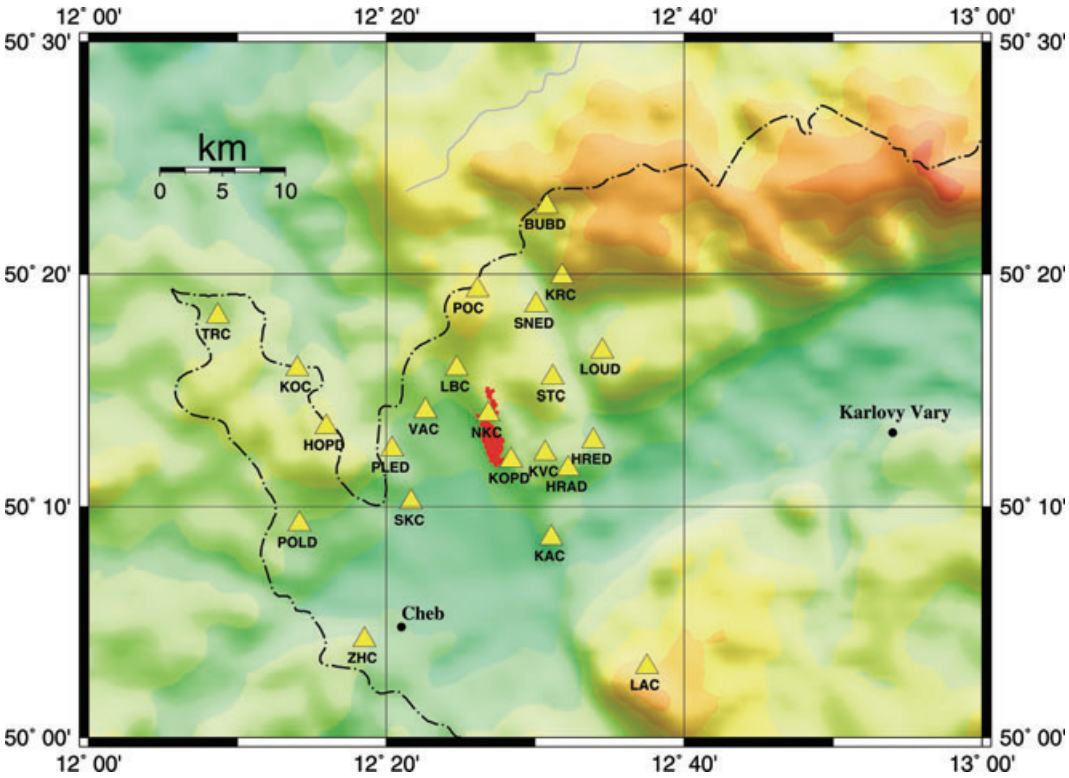

Figure 1. Topographic map of the West Bohemia/Vogtland region. The epicentres of the 2008 swarm earthquakes are marked by red circles, the WEBNET stations are marked by yellow triangles. The dashed-dotted line shows the border between the Czech Republic and Germany.

4 km long cluster striking N170°E. The hypocentres were located at depths of 7.5–11.0 km. The swarm was recorded by 22 three-component short-period seismic West Bohemia Network (WEBNET) stations (Fig. 1) surrounding the swarm epicentres (Fischer *et al*. 2010). The sampling frequency was 250 Hz and the frequency band was flat from 0.5–1.0 to 60–80 Hz depending on the seismometer and the acquisition system used. The epicentral distance of all stations is less than 30 km. Since the earthquakes were recorded by many stations with excellent focal sphere coverage, the data provide a unique opportunity to retrieve focal mechanisms and other source parameters very accurately. The focal mechanisms are basically of two types (Vavryčuk 2011). The majority of events are mostly oblique left-lateral strike slips with one of the nodal lines being oriented nearly in the N–S direction with a strike of 169°. This direction coincides well with the fault plane mapped from the clustering of hypocentres. A small portion of events display oblique right-lateral strike-slip mechanisms with an activated fault in the WNW direction with a strike of 304°. This fault is well manifested on the Earth's surface. The maximum compressive stress determined from the focal mechanisms has an azimuth of N146°E (Vavryčuk 2011).

3 ANALYSIS OF *P* WAVEFORMS

We analyse 12 earthquakes in the magnitude range from 1.6 to 3.7. The hypocentres are concentrated in a small area (see Fig. 1, Table 1) at depths between 7.6 km to 10.8 km. The velocity records were filtered by the bandpass filter with corner frequencies of 1 Hz and 35 Hz. This removed the low- and high-frequency seismic noise in the data and increased the signal-to-noise ratio.

3.1 Observations of waveform complexity

The seismic records display a considerably variable complexity of the *P* waveforms at stations. This is visible, in particular, for the strongest earthquakes with magnitudes 3 or higher. Fig. 2 shows records at six stations for an earthquake with a magnitude of 3.7. The black and red lines show records with simple and complex *P* waveforms, respectively.

The simple *P* waveforms consist typically of a dominant low-frequency pulse. After the pulse, the amplitudes decay very fast. Sometimes, the pulse is not single but can be split reflecting complex rupture history. This case is easily identified because the complexity in the *P* waveform is replicated in the *S* waveform as well.

The complex *P* waveforms are typically of longer duration than simple *P* waveforms and with slow amplitude decay in time. They are more high-frequency and sometimes resemble resonant waves. Interestingly, this complexity of *P* waveforms is not replicated in the *S* waveforms. The high frequencies present in the complex *P* waveforms are missing in the *S* waveforms.

3.2 Waveform complexity as noise or path effect

A straightforward explanation of the differences in the complexity of *P* waveforms is the presence of seismic noise in records, site effects generated by the complex inhomogeneous structure under each station or the scattering of waves at small-scale

Table 1. List of events. ID is the identification of the event, M_L is the local magnitude, M_0 is the scalar seismic moment. The strike, dip and rake angles define the low-frequency focal mechanisms.

No	ID	Date	Time	M_L	Latitude (°)	Longitude (°)	Depth (km)	M_0 (Nm)	Strike (°)	Dip (°)	Rake (°)
1	X5488A	2008 October 14	19:00:33.10	3.7	50.213	12.448	8.9	2.85E+14	161	61	−32
2	X1466A	2008 October 10	03:22:05.26	3.6	50.213	12.446	9.4	1.67E+14	167	70	−27
3	X1590D	2008 October 09	22:20:37.91	3.5	50.215	12.445	9.6	1.14E+14	165	73	−34
4	X5101A	2008 October 14	04:01:36.31	3.0	50.217	12.444	9.7	4.09E+13	167	72	−36
5	X4619A	2008 October 13	01:42:47.36	2.7	50.210	12.451	10.8	1.64E+13	189	59	−39
6	X6683A	2008 October 21	02:14:02.54	2.7	50.221	12.442	9.5	5.50E+13	158	63	−36
7	X874A	2008 October 08	00:14:40.94	2.2	50.209	12.446	10.2	3.61E+12	160	78	–39
8	X957A	2008 October 08	01:27:13.07	2.0	50.204	12.449	10.2	6.25E+12	157	63	–31
9	X1709A	2008 October 10	00:04:54.13	1.8	50.213	12.445	10.0	1.63E+12	349	86	27
10	X2923A	2008 October 10	22:01:53.10	1.6	50.222	12.445	9.1	1.86E+12	351	78	33
11	X499A	2008 October 06	16:33:36.79	1.6	50.206	12.444	10.2	2.86E+11	175	52	−29
12	X1720A	2008 October 10	00:18:51.99	1.6	50.211	12.445	10.1	5.27E+11	203	58	−34

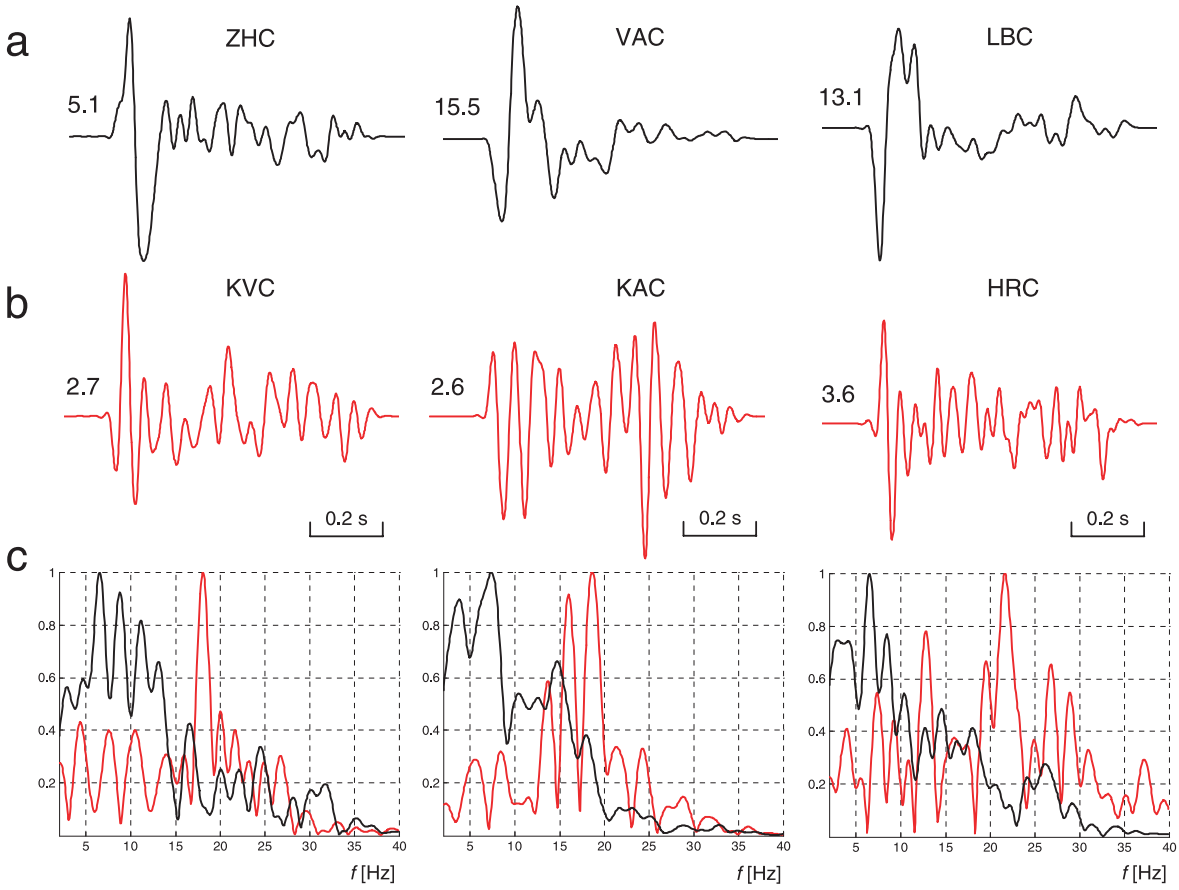

Figure 2. Examples of simple (a) and complex (b) *P* waveforms and the respective normalized amplitude spectra (c) for the $M = 3.7$ earthquake of 2008 October 14 at 19:00:33 (Event 1 from Tab. 1). The time window is 0.9 s. The velocity records are shown; the numbers at the records are the scale factors in 10^{-4} m s^{-1}.

inhomogeneities in the crust (Takemura *et al*. 2009). For example, waves scattered at a shallow subsurface structure can generate differentially complex *P* waveforms at stations. However, neither the presence of seismic noise nor path effects fit our observations. First, all analysed waveforms including stations close to nodal lines have a high signal-to-noise ratio so that the complexity in the *P* waveforms cannot be affected by seismic noise. Secondly, a majority of stations is deployed on hard rocks with no sedimentary cover, so that the site effects should not be dominant. Moreover, the site effects should produce complex waveforms at 'problematic' stations consistently for all events from the same focal area. The same applies to the waveform complexity introduced

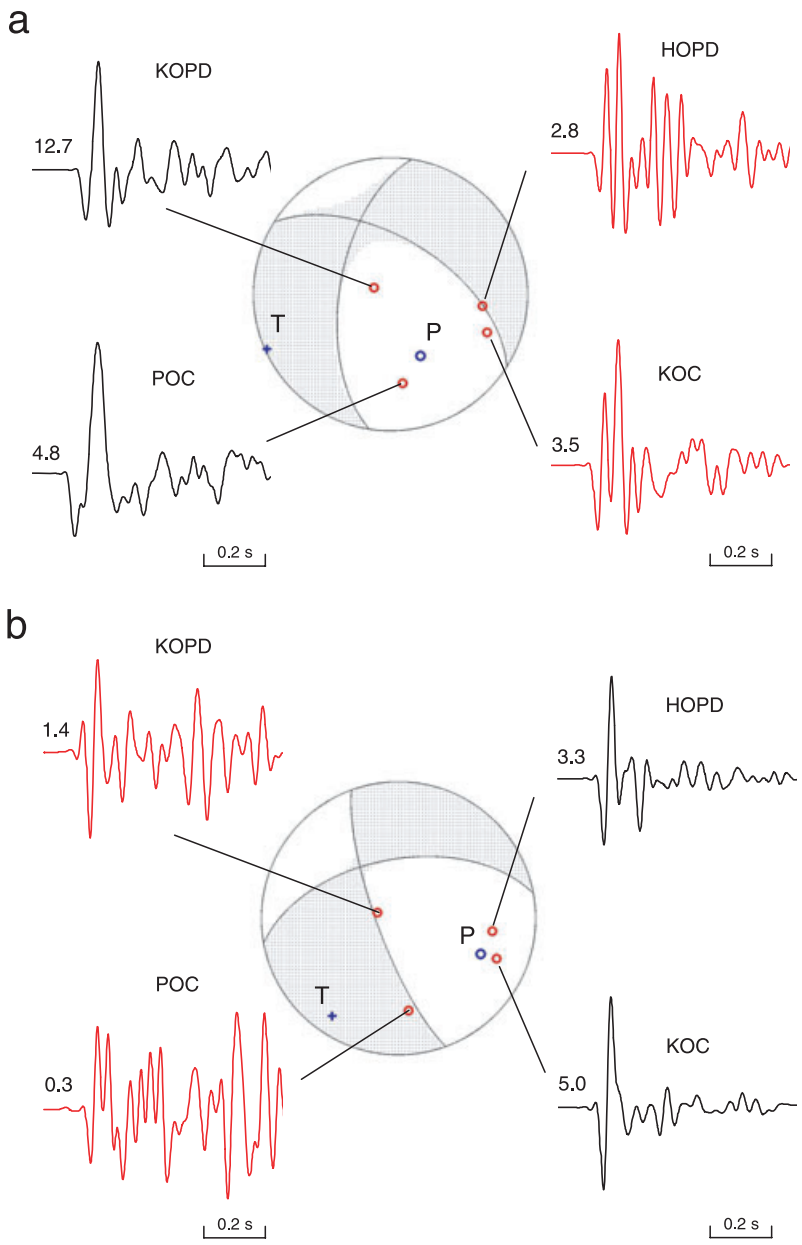

Figure 3. Examples of simple (black) and complex (red) *P* waveforms for: (a) $M = 2.7$ earthquake of 2008 October 13 at 01:42:47 (Event 5), and (b) $M = 2.2$ earthquake of 2008 October 8 at 00:14:41 (Event 7). The time window is 0.75 s. The velocity records are shown; the numbers at the records are the scale factors in 10^{-5} m s^{-1}. For the parameters of the focal mechanisms, see Tab. 1. The blue circle and plus sign show the position of the *P* and *T* axes. The positions of stations are denoted by red circles.

by the scattering of waves at small-scale inhomogeneities in the crust. In this case, the complex waveforms should be observed uniformly for all events and for most stations in a given frequency range.

On the contrary, Figs 3(a) and (b) show that earthquakes from the same focal area can generate simple as well as complex waveforms at the same station. The figure shows focal mechanisms for two events calculated using the moment tensor inversion described in Vavryčuk (2011), and the waveforms observed at stations KOC, POC, HOPD and KOPD. The waveforms of the first event are simple at stations POC and KOPD but complex at stations KOC and HOPD. The waveforms of the other event have exactly opposite properties: they are complex at stations POC and KOPD but simple at stations KOC and HOPD. This observation excludes the paths effects as a major origin of the waveform complexity.

3.3 Waveform complexity due to complex rupture history or source directivity

The observation of differently complex waveforms radiated in different ray directions from the source is inconsistent with the simple

point dislocation source model with a common source-time function. This model should produce the same level of complexity of waveforms recorded at all stations. For simple/complex rupture histories, the waveforms should be uniformly simple/complex. The observation is inconsistent also with the model of a finite source with unilateral rupturing generating the directivity effect in the radiated waves. The directivity effect would explain the frequency shifts in waves radiated in different directions, but the waveforms should be similar, displaying the same level of complexity (Cipar 1979, Lay & Wallace 1995).

3.4 Waveform complexity due to complex shear–tensile motions

The positions of stations on the focal sphere in Fig. 3 indicate that the waveform complexity is dependent on the source mechanism. The stations with complex waveforms are in directions very close to nodal lines, while stations with simple waveforms are in directions far from the nodal lines. Hence, the waveform complexity observed at a station depends on the focal mechanism of the event. The peculiarities in the observed data might point to a

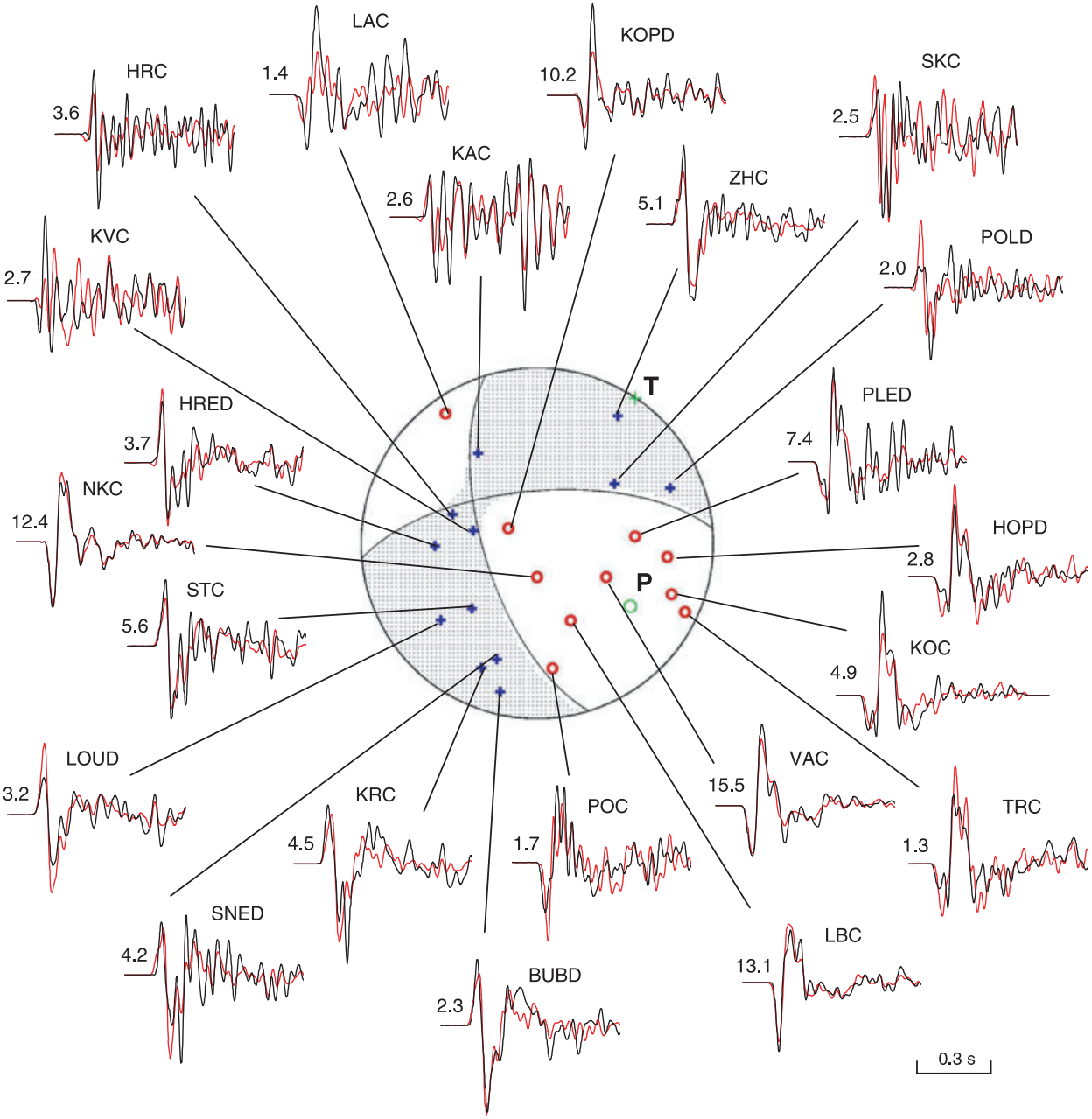

Figure 4. Inversion for the focal mechanism from *P* waveforms for the $M = 3.7$ earthquake of 2008 October 14 at 19:00:33 (Event 1). Black line, observed waveforms; red line, synthetic waveforms; red circles, stations with minus *P*-wave polarities; blue crosses, stations with plus *P*-wave polarities. The time window is 0.75 s. The velocity records are shown; the numbers at the records are the scale factors in 10^{-4} m s^{-1}.

source model, combining shear and tensile faulting with source-time functions characterized by different frequencies and by a different level of complexity. If the shear and tensile radiation functions are different, the waveforms will vary with ray directions from the source.

Next, we shall invert the analysed events for the complex shear–tensile source-time functions and study the properties of the shear and tensile motions separately. Finally, we shall verify the inversion results using numerical modelling.

4 MOMENT TENSOR INVERSION FOR SHEAR–TENSILE SOURCE-TIME FUNCTIONS

The shear and tensile source-time functions are calculated using the full moment tensor inversion from waveforms. In the inversion, we use the velocity records of the vertical component of direct *P* waves with duration of 0.25–0.75 s depending on the magnitude of the event. The Green functions are calculated for a vertically inhomogeneous velocity model using the ray method (Červený 2001) and incorporate effects of the Earth's surface. The moment tensor inversion is performed in the frequency domain using the generalized linear inversion. The inversion involves two steps. First, the data are inverted in the frequency range of 1–8 Hz. The common source-time function is obtained by averaging the six normalized moment-time functions. The scale factors of the moment-time functions to the common source-time function form a time-independent seismic moment tensor in the low-frequency approximation. The retrieved seismic moment tensor is decomposed into the DC and non-DC parts (Vavryčuk 2001, 2002), and the DC part is used to calculate the fault coordinate system. Secondly, the six moment-time functions are calculated in the whole frequency range of 1–35 Hz. In general, they are mutually different functions of time. The averaging procedure for extracting a common source-time function is no longer applied. The moment-time functions are rotated into the fault coordinate system, to separate the moment-time functions responsible for shear and tensile faulting. The shear component is identified with the off-diagonal moment-time function, while the tensile component is calculated as the trace of the diagonal moment-time functions.

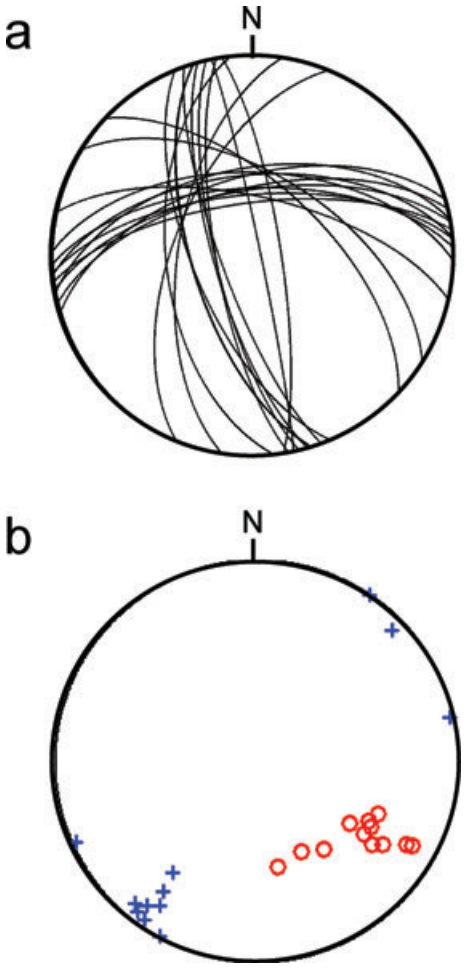

Figure 5. Nodal lines (a) and *P*/*T* axes (b) of the focal mechanisms for the 12 analysed events. The *P* and *T* axes are denoted by red circles and blue plus signs, respectively. For the parameters of the focal mechanisms, see Table 1.

5 ANALYSIS OF THE SOURCE-TIME FUNCTIONS

Fig. 4 shows the results of the inversion of the $M = 3.7$ earthquake (Event 1 from Table 1). First, the figure demonstrates how well the synthetic waveforms fit the observed data. Secondly, it demonstrates how the waveform complexity depends on the station position on the focal sphere. Stations positioned near the P/T axes (stations VAC, LBC, NKC, KOC, TRC and ZHC) have rather simple and low-frequency waveforms with a predominant pulse. The waveforms become more complex and more high frequency if the position of the station is close to the nodal lines (stations KAC, SKC, HRC, KVC and STC). As mentioned above, this is an indication that the source process cannot be described by one common source-time function. While a low-frequency source-time function is dominant in areas of maximum radiation of shear faulting, the high-frequency source-time function becomes visible in directions of suppressed shear radiation.

Figs 5 and 6 show the results of the moment tensor inversion of 12 selected earthquakes. Fig. 5 shows the low-frequency shear focal mechanisms (the first step in the moment tensor inversion). Fig. 6 shows the moment-time rate functions and their normalized amplitude spectra calculated in the whole frequency range (the second step in the moment tensor inversion). The figure indicates a different form and a different frequency content of the shear (black line) and tensile (red line) moment-time rate functions. The tensile functions have lower amplitudes and higher frequencies than the shear functions. The shear functions have predominantly frequencies less than 10 Hz. The predominant frequency governs the scaling law being dependent on the source dimension. The tensile functions display typically a narrow frequency band with frequencies around 20 Hz and with no apparent dependence on the source dimension.

Since the shear functions have higher amplitudes, the radiation of shear faulting is dominating. This concerns, in particular, the directions near the *P* and *T* axes, where the radiation of shear faulting is most intense. However, the dominance of shear faulting is lost in directions near the nodal lines. In these directions, tensile faulting becomes significant. Tensile faulting is associated with volume changes in the source producing a more

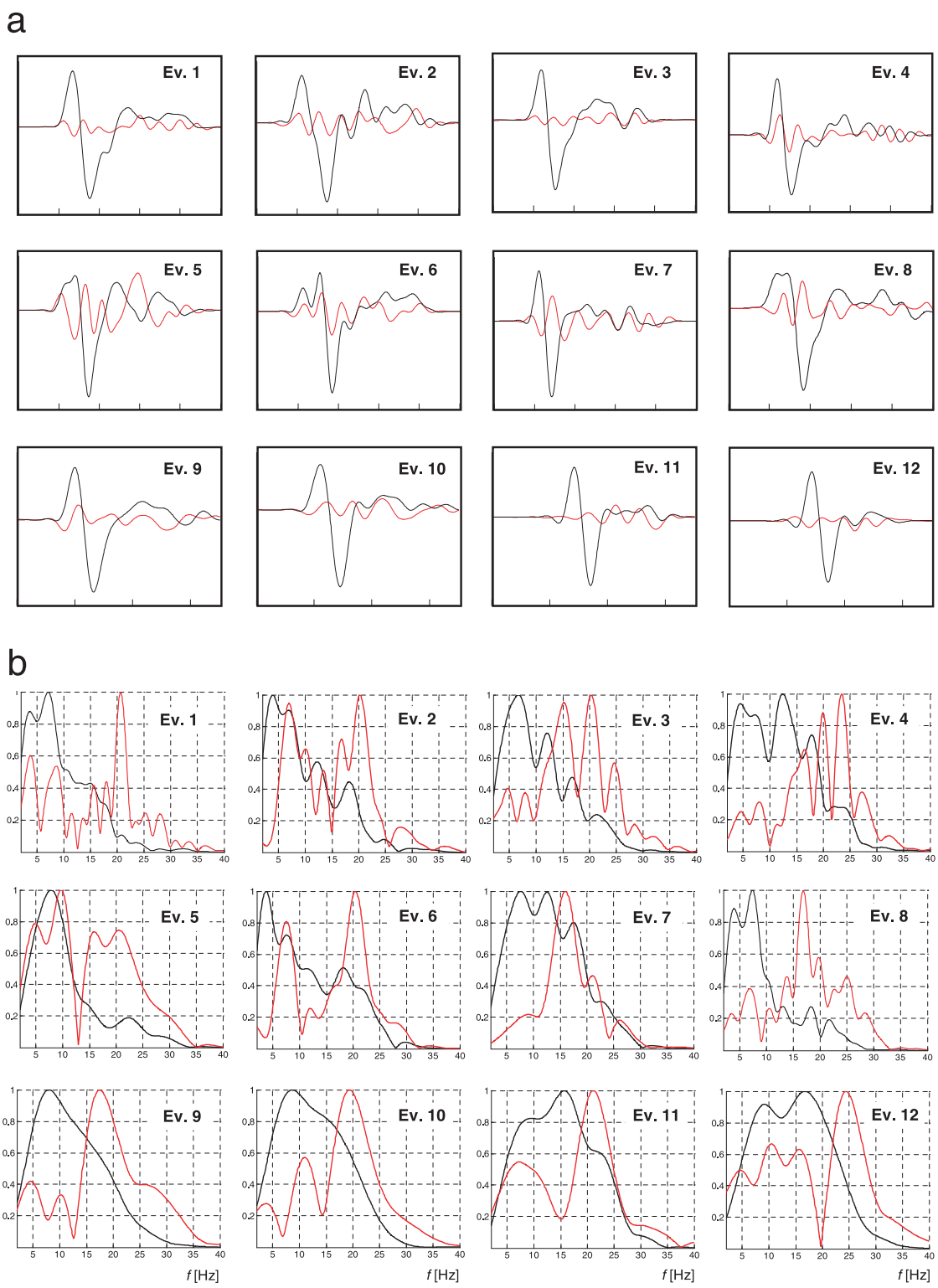

Figure 6. Moment-time rate functions (a) and their normalized amplitude spectra (b) for the 12 analysed earthquakes. The moment-time rate functions are defined as the second time derivatives of the moment-time functions (i.e., slip accelerations). Black/red line, shear/tensile moment-time rate function. The time scale is in 0.1 s. Detailed information on events is in Table 1.

homogeneous radiation over the whole focal sphere including the nodal lines of the shear focal mechanism. Obviously, a different character of shear and tensile source-time functions projects into the varying complexity of radiated waves with respect to the position of stations on the focal sphere. At stations near the P/T axes, the waveforms resemble more the shear source-time function. At stations near the nodal lines, the waveforms resemble the tensile source-time function.

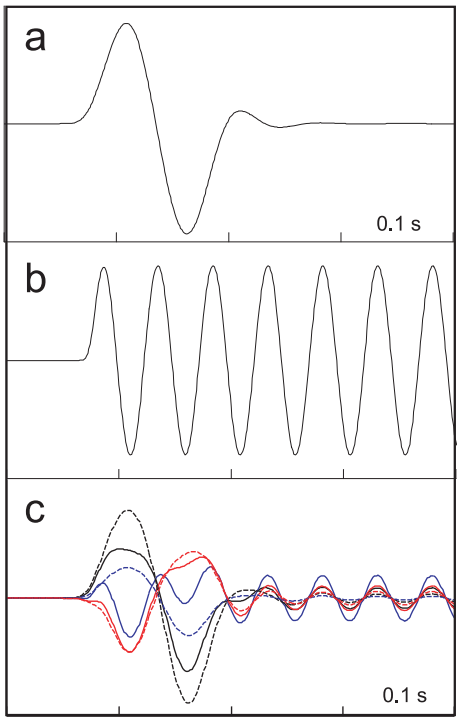

Figure 7. Synthetic moment-time rate functions. Normalized shear (a) and tensile (b) moment-time rate functions are shown in the fault coordinate system. The complete moment-time rate functions (c) are shown in the standard geographical system (x_1 – north, x_2 – east, x_3 – downwards). The M_{11}, M_{22} and M_{33} functions are marked by black, blue and red full lines, the M_{12}, M_{13} and M_{23} functions are marked by black, blue and red dashed lines, respectively.

6 SHEAR FAULTING WITH TENSILE VIBRATIONS: NUMERICAL MODELLING

In this section, we try to support the obtained results using numerical modelling. We construct a synthetic shear-tensile source model similar to that retrieved from observations. The model is composed of low-frequency shear faulting and high-frequency tensile vibrations occurring on the same fault. We calculate a radiated wavefield and invert back for the moment-time functions. In this way, we check the robustness of the inversion scheme and the reliability of the results.

The velocity model, station configuration and event location are identical with those used for the inversion of Event 1 (see Fig. 4). Similarly, the shear focal mechanism is identical with that obtained from the low-frequency inversion of Event 1 (see Tab. 1). According to the stress analysis by Vavryčuk (2011), the fault plane is identified with the nodal plane with a strike of 163°. The synthetic shear and tensile moment-time rate functions are shown in Fig. 7 and roughly mimic the retrieved moment-time rate functions in Fig. 6(a). The radiated wavefield is calculated using the same Green's functions as used in the inversion. For simplicity, no noise and no errors in the location and velocity model are introduced in the inversion.

Figs 8(a) and (b) show a comparison of the inversion from real observations and from synthetic data. The upper plots show the focal mechanisms retrieved for the frequency range of 1–8 Hz. Both focal mechanisms are slightly non-DC probably due to the presence of the tensile vibrations not fully cut off in the low-frequency inversion. The non-DC components for real and synthetic data attain values of 15 per cent and 4 per cent, respectively. The lower plots show the moment-time rate functions in the time and frequency domains in the fault coordinate system retrieved for the frequency range of 1–35 Hz. The synthetic test reveals that the shear and tensile functions are well reproduced. Nevertheless, the synthetic shear function is not reproduced exactly being contaminated by high-frequency vibrations at later times, where no shear motion was assumed in the model (see Fig. 7a).

Figs 9(a) and (b) show a comparison of the inversion from real observations and from synthetic data performed in the frequency range of 20–35 Hz, where only tensile vibrations should be present. The inversion is performed for the very beginning of the signal with duration of 0.25 s. Since the moment tensor inversion often becomes unstable for high frequencies, the results are less reliable than those of the previous inversions. Nevertheless, the synthetic inversion yields robust results even in this case. The retrieved focal mechanism has 99 per cent of the non-DC components and 1 per cent of the DC component indicating almost pure tensile faulting. Also the position of the *T* axis indicates the pure tensile mechanism, because the *T* axis matches the direction of the fault normal exactly (for the relation between the fault normal and the *T* axis for tensile earthquakes, see Vavryčuk 2001). As regards the *P* axis, its position has no physical meaning for tensile motions. It reflects the orientation of the negligible DC component in the mechanism only. Since the DC component is produced by numerical errors in the inversion, the position of the *P* axis is unstable. As regards the observed data, the high-frequency inversion also shows significant non-DC components, but not as high as in the synthetic test. The percentage of the non-DC component is 49 per cent but this value is rather unstable. Similarly as for the synthetic data, the *T* axis is close to the fault normal. This indicates that the high-frequency motions are significantly tensile.

7 CONCLUSIONS

Based on the analysis of *P* waveforms of microearthquakes in West Bohemia we draw the following conclusions:

(1) The standard source model with a common source-time function might be too simplistic and only a rough approximation of the true source model. A more adequate model is the shear-tensile source model with different source-time functions for shear and tensile motions.

(2) The retrieved character of faulting depends on the frequency band of analysed waves. Earthquakes can display apparently simple shear focal mechanisms in the low-frequency band but complex shear-tensile mechanisms if high frequencies are analysed. The source complexity retrieved for high frequencies need not be spurious, being numerical errors of the inversion, but it can be of physical nature.

(3) The tensile vibrations of the fault complicate *P* waveforms. They are associated with volume changes in the source producing a more homogeneous radiation pattern over the whole focal sphere than shear faulting (see Fig. 10). Therefore, the tensile vibrations are visible, particularly, in directions near the nodal lines, where the dominance of the shear radiation is lost.

(4) The shear and tensile motions can have significantly different frequencies. Observations in West Bohemia indicate that the tensile source-time function is usually of a narrow frequency band and of

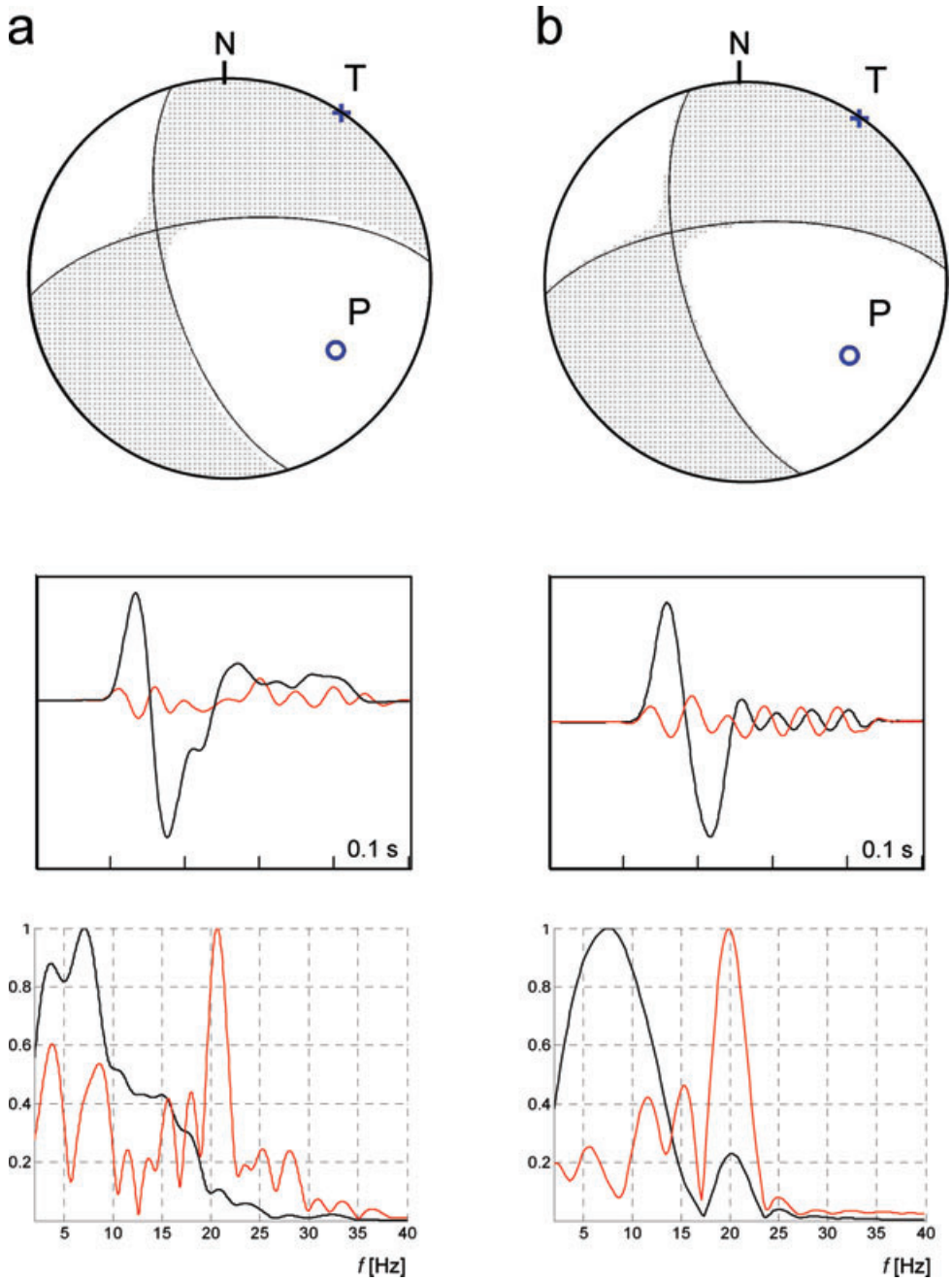

Figure 8. Inversion from real (a) and synthetic (b) data for Event 1. Upper plots, focal mechanisms in the frequency range of 1–8 Hz; middle plots, shear (black line) and tensile (red line) moment-time rate functions retrieved in the frequency range of 1–35 Hz and rotated into the fault coordinate system; lower plots, normalized amplitude spectra of shear (black line) and tensile (red line) moment-time rate functions. The blue circles and plus signs in the upper plots denote the *P* and *T* axes.

higher frequencies than the shear source-time function (Fig. 11). The tensile motions decay rather slowly with time.

(5) Since the tensile vibrations are of high frequency, they are more pronounced in records of acceleration and velocity rather than in records of displacement.

(6) The tensile vibrations might be generated by the opening of the fault during shear rupturing or by creating wing tensile cracks at the tip of the fault when shear rupturing stops (Fig. 12).

(7) The final static displacement produced by tensile vibrations can be zero or negligible. The tensile vibrations do not necessarily cause permanent volume changes in the source such as a permanent extension (opening) or compression (closing) of the fault.

(8) The transient displacement produced by tensile vibrations is small being at least 15–20 times less than the maximum slip attained during shear faulting. For example, for an average shear slip of 10 cm along a fault, the average tensile displacement should be less than 0.5 cm on the same fault. If tensile vibrations are produced by a small fault segment only (e.g. wing cracks), the amplitudes of tensile vibrations should be proportionally higher.

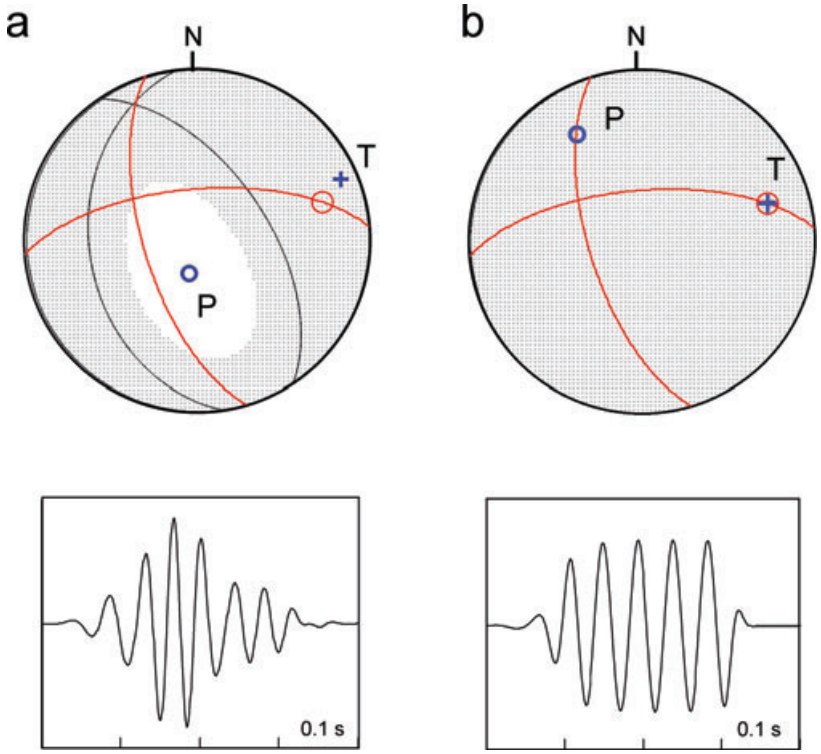

Figure 9. Inversion for high-frequency vibrations from real (a) and synthetic (b) data for Event 1. Upper plots, focal mechanisms in the frequency range of 20–35 Hz; lower plots, tensile moment-time rate functions retrieved in the frequency range of 20–35 Hz. The blue circles and plus signs in the upper plots denote the *P* and *T* axes. The red nodal lines correspond to the mechanism retrieved for frequencies between 1 and 8 Hz. The black nodal lines in (a) correspond to the high-frequency DC mechanism. No nodal lines of the high-frequency DC mechanism are shown in (b), because the DC part is negligible. The open red circle denotes the position of the fault normal.

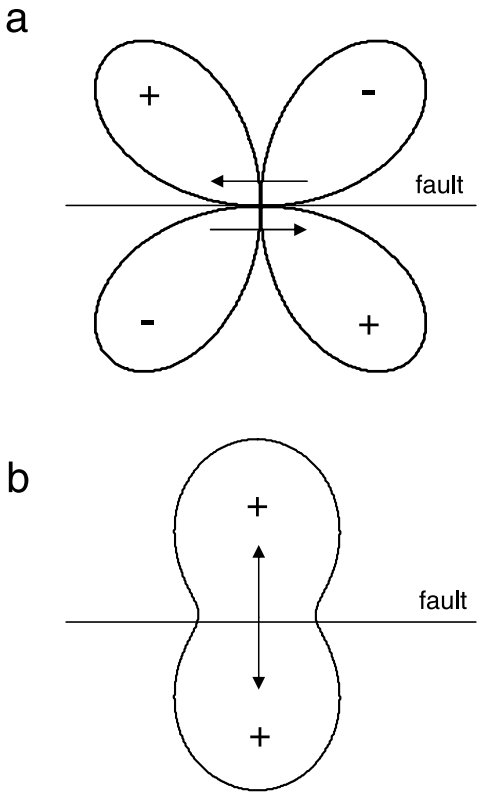

Figure 10. *P*-wave radiation patterns of shear (a) and tensile (b) faulting. The arrows show the direction of the motion at the source. The signs indicate the polarity of the *P* wave. The *P* to *S* velocity ratio is 1.73 in (b).

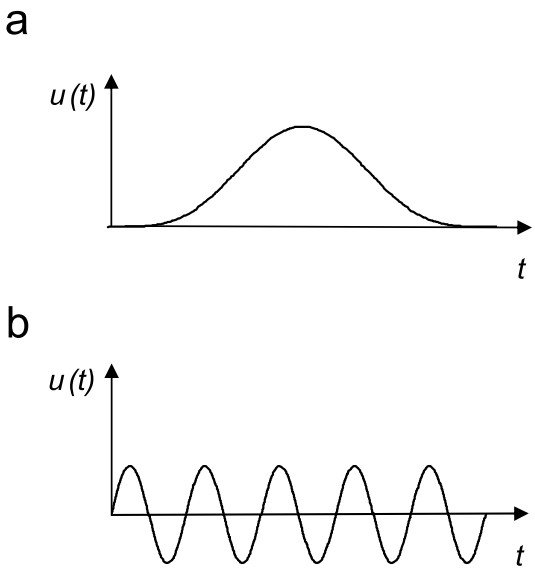

Figure 11. Sketch of the first time derivative of the shear (a) and tensile (b) source-time functions. The grey arrows in (b) and (c) show the predominant shear motion.

(9) A detailed study of the tensile source-time functions can provide new information on the physical processes in the source and on the properties of rocks on the fault.

Obviously, the general validity of the conclusions should be proved by studies in other tectonic environments.

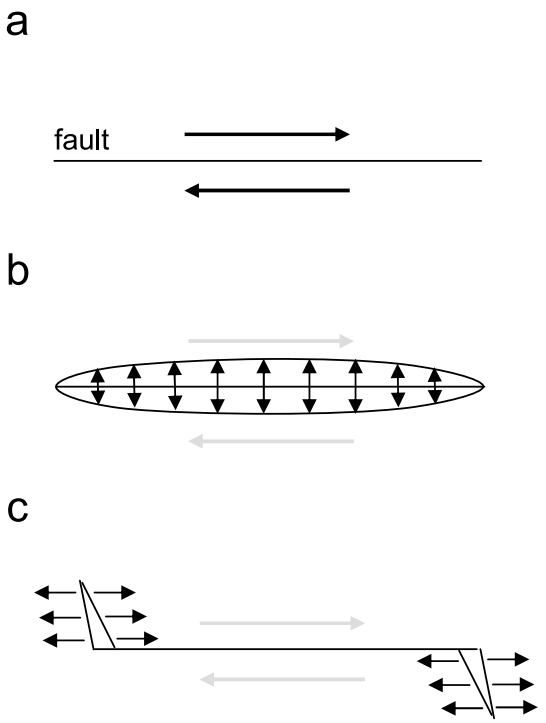

Figure 12. Sketch of the different character of shear and tensile motions of the fault. (a) Shear motion on the fault, (b) tensile motion on the fault, (c) tensile motion on the wing tensile cracks. The arrows show the direction of the motion.

ACKNOWLEDGMENTS

I thank two reviewers for their constructive reviews, Pavla Hrubcová for help with preparing Fig. 1 and for many fruitful discussions of the topic, and Alena Boušková, Tomáš Fischer and Josef Horálek for providing me with the WEBNET data and for help with their processing. The work was supported by the Grant Agency of the Academy of Sciences of the Czech Republic, Grant No. IAA300120801, by the Grant Agency of the Czech Republic, Grant No. P210/10/2063 and by the European Community's FP7 Consortium Project AIM 'Advanced Industrial Microseismic Monitoring', Grant Agreement No. 230669.

REFERENCES

Aki, K., 1984. Asperities, barriers, characteristic earthquakes and strong motion prediction, *J. Geophys. Res.,* **89,** 5867–5872.

Babuška, V., Plomerová, J. & Fischer, T., 2007. Intraplate seismicity in the western Bohemian Massif (central Europe): a possible correlation with a paleoplate junction, *J. Geodyn.,* **44,** 149–159.

Boatwright, J., 2007. The persistence of directivity in small earthquakes, *Bull. seism. Soc. Am.,* **97**, 1850–1861.

Červený, V., 2001. *Seismic Ray Theory,* Cambridge University Press, Cambridge.

Cipar, J., 1979. Source process of the Haicheng, China earthquake from observsations of P and S waves, *Bull. seism. Soc. Am.,* **69**, 1903–1916.

Cohee, B.P. & Beroza, G.C., 1994. Slip distribution of the 1992 Landers earthquake and its implications for earthquake source mechanics, *Bull. seism. Soc. Am.,* **84**, 693–712.

Dufumier, H. & Rivera, L., 1997. On the resolution of the isotropic component in moment tensor, *Geophys. J. Int.,* **131**, 595–606.

Fischer, T., 2003. The August-December 2000 earthquake swarm in NW Bohemia: the first results based on automatic processing of seismograms, *J. Geodyn.,* **35,** 59–81.

Fischer, T. & Horálek, J., 2003. Space-time distribution of earthquake swarms in the principal focal zone of the NW Bohemia/Vogtland seismoactive region: period 1985–2001, *J. Geodyn.,* **35,** 125–144.

Fischer, T., Horálek, J., Michálek, J. & Boušková, A., 2010. The 2008 West Bohemia earthquake swarm in the light of the WEBNET network, *J. Seismol.,* **14,** 665–682.

Foulger, G.R., Julian, B.R., Hill, D.P. Pitt, A.M., Malin, P. & Shalev, E., 2004. Non-double-couple microearthquakes at Long Valley caldera, California, provide evidence for hydraulic fracturing, *J. Volc. Geotherm. Res.,* **132,** 45–71.

Frez, J., Nava, F.A. & Acosta, J., 2010. Source rupture plane determination from directivity doppler effect for small earthquakes recorded by local networks, *Bull. seism. Soc. Am.,* **100,** 289–297.

Frohlich, C., 1994. Earthquakes with non-double-couple mechanisms, *Science,* **264,** 804–809.

Julian, B.R., Miller, A.D. & Foulger, G.R., 1997. Non-double-couple earthquake mechanisms at the Hengill–Grensdalur volcanic complex, southwest Iceland, *Geophys. Res. Lett.*, **24,** 743–746.

Julian, B.R., Miller, A.D. & Foulger, G.R., 1998. Non-double-couple earthquakes 1: Theory, *Rev. Geophys.,* **36,** 525–549.

Kikuchi, M. & Kanamori, H., 1984. Inversion of complex body waves, *Bull. seism. Soc. Am.,* **72,** 491–506.

Konca, A.O., Leprince, S., Avouac, J.-P. & Helmberger, D.V., 2010. Rupture process of the 1999 Mw 7.1 Duzce earthquake from joint analysis of SPOT, GPS, InSAR, strong-motion, and teleseismic data: a supershear rupture with variable rupture velocity, *Bull. seism. Soc. Am,* **100,** 267–288.

Lay, T. & Wallace, T.C., 1995. *Modern Global Seismology,* Academic Press, New York, NY.

Lay, T., *et al*. 2005. The great Sumatra-Andaman earthquake of 26 December 2004. *Science,* **308,** 1127–1133.

Madariaga, R., Adda-Bedia, M. & Ampuero, J.P., 2006. Seismic radiation from simple models of earthquakes, *Geophys. Monogr.,* **170,** 223–236, doi:10.1029/170GM07.

Miller, A.D., Foulger, G.R. & Julian, B.R., 1998. Non-double-couple earthquakes 2: observations, *Rev. Geophys.,* **36,** 551–568.

Mori, J., 1996. Rupture directivity and slip distribution of the M 4.3 foreshock to the 1992 Joshua tree earthquake, Southern California, *Bull. seism. Soc. Am.,* **86,** 805–810.

Ross, A.G., Foulger, G.R. & Julian, B.R., 1996. Non-double-couple earthquake mechanisms at the Geysers geothermal area, California, *Geophys. Res. Lett.,* **23,** 877–880.

Seekins, L.C. & Boatwright, J., 2010. Rupture directivity of moderate earthquakes in Northern California, *Bull. seism. Soc. Am.,* **100,** 1107–1119.

Spudich, P. & Frazer, N., 1984. Use of ray theory to calculate high-frequency radiation from earthquake sources having spatially variable rupture velocity and stress drop, *Bull. seism. Soc. Am.,* **74,** 2061–2082.

Takemura, S., Furumura, T. & Saito, T., 2009. Distortion of the apparent S-wave radiation pattern in the high-frequency wavefield: Tottori-Ken Seibu, Japan, earthquake of 2000, *Geophys. J. Int.,* **178,** 950–961.

Vavryčuk, V., 1993. Crustal anisotropy from local observations of shear-wave splitting in West Bohemia, Czech Republic, *Bull. seism. Soc. Am.,* **83,** 1420–1441.

Vavryčuk, V., 2001. Inversion for parameters of tensile earthquakes, *J. Geophys. Res.,* **106,** B8, 16.339–16.355, doi: 10.1029/2001JB000372.

Vavryčuk, V., 2002. Non-double-couple earthquakes of January 1997 in West Bohemia, Czech Republic: Evidence of tensile faulting, *Geophys. J. Int.,* **149,** 364–373, doi:10.1046/j.1365-246X.2002.01654.x.

Vavryčuk, V., 2011. Principal earthquakes: theory and observations from the 2008 West Bohemia swarm, *Earth planet. Sci. Lett.,* **305,** 290–296, doi:10.1016/j.epsl.2011.03.002.

Wald, D. J., 1996. A dislocation model of the 1995 Kobe, Japan earthquake determined from strong motion, teleseismic, and geodetic data, *J. Phys. Earth,* **44,** 489–503.

Zeng, Y. & Chen, Ch.-H., 2001. Fault rupture process of the 20 September 1999 Chi-Chi, Taiwan, earthquake, *Bull. seism. Soc. Am.,* **91,** 1088–1098.